CHEMISTRY OF MATERIALS

pubs.acs.org/cm

Article

Open Access

This article is licensed under CC-BY 4.0

Competing Magnetic Ground States in Ilmenite-Type High-Entropy Oxides

Published as part of Chemistry of Materials special issue "Celebrating Myung-Hwan Whangbo on the Occasion of his 80th Birthday".

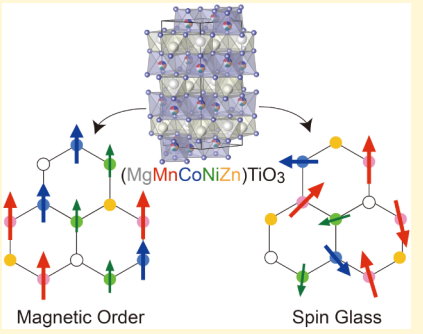
Damian Contant,* Sebastian Bette,* Robert Dinnebier,* Ivan da Silva, Diana Dragoe, Nita Dragoe, Hidenori Takagi,* and Tomohiro Takayama*

Cite This: https://doi.org/10.1021/acs.chemmater.6c01899

Read Online

ACCESS | Metrics & More | Article Recommendations | Supporting Information

ABSTRACT: High-entropy oxides containing more than five different cations have emerged as platforms for diverse functionalities, including magnetism. We synthesized a high-entropy oxide with an ilmenite-type structure $(Mg_{0.2}Mn_{0.2}Co_{0.2}Ni_{0.2}Zn_{0.2})TiO_3$ and revealed that it undergoes long-range antiferromagnetic ordering below $T_N \sim 9.5$ K despite strong cation disorder. Neutron diffraction measurements showed that the magnetic structure comprises ferromagnetic honeycomb planes that stack antiferromagnetically, analogous to those of the parent $CoTiO_3$ and $NiTiO_3$ ilmenites. Derivatives of the high-entropy ilmenite were obtained by substituting one of the divalent cations of $(Mg_{0.2}Mn_{0.2}Co_{0.2}Ni_{0.2}Zn_{0.2})TiO_3$ with an equimolar amount of Li^+ ions and trivalent cations. The antiferromagnetic order remains robust against aliovalent doping that introduces extra disorder owing to cations with different valence states. In contrast, when the cation ratio was tuned to a Mn-rich composition of $(Mg_{0.2}Mn_{0.3}Co_{0.15}Ni_{0.15}Zn_{0.2})TiO_3$, spin-glass freezing was observed, most likely because of the enhanced competition between the in-plane magnetic interactions. This suggests that long-range magnetic ordering in high-entropy materials is formed by a subtle balance of competing interactions, and fine-tuning of constituent magnetic ions provides control over their magnetic ground states.



1. INTRODUCTION

The entropy stabilization of complex, multi-component materials was initially proposed for alloys, giving birth to a class of materials called high-entropy alloys.[1,2] The concept of entropy stabilization was later applied to other classes of materials, such as oxides. A rocksalt-type oxide with more than five different cations, $(Mg_{0.2}Co_{0.2}Ni_{0.2}Cu_{0.2}Zn_{0.2})O$ (denoted as (MgCoNiCuZn)O hereafter), has appeared as the first high-entropy oxide (HEOx).[3] The successful synthesis of rocksalt-type HEOx has prompted the search for other complex HEOx, such as perovskite, spinel, and fluorite-type compounds.[4] In parallel with the development of materials, HEOx have been shown to display unexpected functionalities. For example, the rocksalt HEOx exhibits a colossal dielectric constant[5] and high ionic conductivity upon alkali-metal doping.[6] In addition, various properties ranging from high-performance electrochemical functions,[7,8] catalytic activities,[9] and thermoelectric properties[10] have been reported for high-entropy oxides and other high-entropy ceramics.

As HEOx often contain magnetic cations such as Co^{2+} and Ni^{2+}, they may display unique magnetic properties. At a glance, the strong cation disorder of HEOx would be considered to simply lead to spin-glass freezing. As opposed to this view, the rocksalt-type HEOx (MgCoNiCuZn)O was revealed to undergo long-range antiferromagnetic ordering below ~120 K[11,12]. The presence of long-range magnetic order in such a disordered material is surprising, and the wide variety of compositional spaces in HEOx should enable the fine control of their magnetic properties and functionalities. Following the discovery of the long-range magnetic order in the rocksalt HEOx, the magnetic properties and functions of other HEOx have been extensively investigated.[13−16]

One of the key features of HEOx in terms of magnetism is the presence of multiple magnetic cations with different electronic configurations, which should result in the coexistence of different magnetic exchange interactions, namely, bond-disorder in magnetic interactions. In the case of the rocksalt (MgCoNiCuZn)O, the dominant magnetic exchange coupling is antiferromagnetic between the second-nearest neighbor cations in the 180° bond.[17] This dominant exchange path is identical to that of binary rocksalt oxides such as CoO

Received: June 30, 2026
Revised: August 28, 2026
Accepted: August 31, 2026

ACS Publications

© XXXX The Authors. Published by American Chemical Society

Downloaded from pubs.acs.org/cmatex/article-pdf/doi/10.1021/acs.chemmater.6c01899/6839719/acs.chemmater.6c01899.pdf by NATL INST FOR MATLS SCIENCE (NIMS) user on 11 September 2026

and NiO, which reasonably explains why the high-entropy rocksalt oxides have a similar magnetic structure to the binary oxides.[11,12] To explore potential rich magnetic ground states of HEOx, complex magnetic interactions, distinct from those of the parent compounds containing a single magnetic ion, may need to be incorporated.

We therefore focused on $MTiO_3$ ilmenite-type oxides (Figure 1a), where M represents a collection of various divalent cations. In ilmenite $MTiO_3$, different magnetic structures are observed depending on the nature of the M^{2+} cations; $MnTiO_3$ forms a Néel-type antiferromagnetic order,[18] whereas the magnetic moments in $CoTiO_3$ and $NiTiO_3$ order ferromagnetically within the honeycomb *ab*-planes and the ferromagnetic planes stack antiferromagnetically along the *c*-axis,[18,19] which is often called A-type antiferromagnetic order. This difference is attributable to the distinct magnetic exchange coupling of the M^{2+} cations. The magnetic moments of Mn^{2+} ions with a $3d^5$ high-spin configuration ($S = 5/2$) couple antiferromagnetically through the direct exchange of t_{2g} electrons across the edges of the MnO_6 octahedra in the honeycomb lattice. On the other hand, the ferromagnetic interaction of e_g electrons in the 90° M−O−M bonds is predominant for Co^{2+} ($3d^7$ high-spin configuration) and Ni^{2+} ($3d^8$) ions. Therefore, by forming a high-entropy configuration at the M-site of the ilmenite $MTiO_3$ phase, competing magnetic exchange interactions can occur within the M^{2+} honeycomb lattice.

We synthesized a high-entropy ilmenite $(Mg_{0.2}Mn_{0.2}Co_{0.2}Ni_{0.2}Zn_{0.2})TiO_3$ (hereafter denoted as $(MgMnCoNiZn)TiO_3$). This high-entropy ilmenite undergoes long-range antiferromagnetic ordering below 9.5 K, despite the chemical disorder and the resultant bond-disorder in the magnetic interactions. Our neutron diffraction measurements revealed that the magnetic structure of $(MgMnCoNiZn)TiO_3$ is similar to that of $CoTiO_3$ and $NiTiO_3$, suggesting that ferromagnetic super-exchange interactions are dominant in the honeycomb planes. Furthermore, a wide variety of high-entropy ilmenites have been synthesized by replacing one of the M cations of $(MgMnCoNiZn)TiO_3$ with an equimolar amount of Li^+ and a trivalent cation, which retains long-range magnetic order, albeit with enhanced chemical disorder. By contrast, spin-glass behavior was observed in the non-equimolar sample of $(Mg_{0.2}Mn_{0.3}Co_{0.15}Ni_{0.15}Zn_{0.2})TiO_3$, where the competition between the in-plane antiferromagnetic and ferromagnetic interactions is likely the most pronounced. This suggests a subtle balance of magnetic interactions and the high tunability of the magnetic ground states of high-entropy materials.

2. EXPERIMENTAL SECTION

2.1. Synthesis

The high-entropy ilmenite $(MgMnCoNiZn)TiO_3$ was synthesized via a conventional solid-state reaction. Powders of MgO (99.99%, Sigma-Aldrich), MnO (99.99%, Thermo Fisher Scientific), Co_3O_4 (99.97+%, ChemPUR), NiO (99.99%, Sigma-Aldrich), ZnO (99.999%, Thermo Fisher Scientific), and TiO_2 (>99.98%, Sigma-Aldrich) were used without further purification. The powders were weighed in the desired ratios and mixed in an agate mortar. The mixture was pelletized and heated at 1100 °C for 24 h in air, and then quenched to room temperature. To examine the possible influence of oxygen non-stoichiometry, the $(MgMnCoNiZn)TiO_3$ samples were annealed at 1100 °C under different atmospheres, such as air, argon or oxygen gas flow, and then cooled to room temperature using a furnace-cooling procedure (the cooling rate was approximately 100 °C/hour). For the aliovalent-doped samples, in addition to the chemicals listed above, powder of Li_2CO_3 (99.995%, ChemPUR), together with Fe_2O_3 (99.995%, Thermo Fisher Scientific), Sc_2O_3 (99.999%, Thermo Fisher Scientific), or In_2O_3 (99.994%, Thermo Fisher Scientific) powder, was added instead of one of the binary oxides shown above.

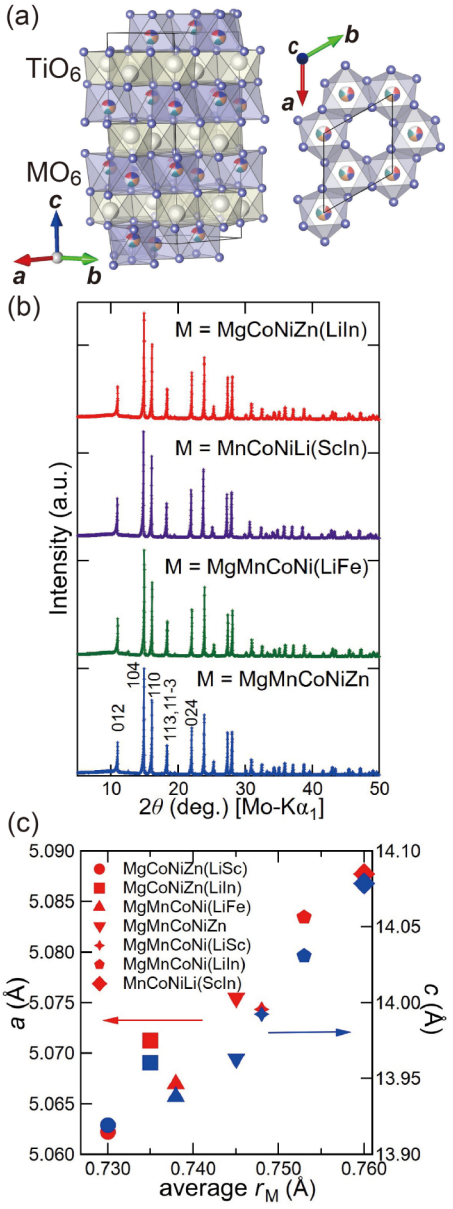


Figure 1. (a) Crystal structure of high-entropy ilmenites $MTiO_3$. The right figure depicts the honeycomb lattice composed of MO_6 octahedra in the *ab*-plane. The structures were visualized using the VESTA software.[48] (b) Powder X-ray diffraction patterns of high-entropy ilmenites $MTiO_3$ collected with Mo−Kα_1 radiation, where M denotes $Mg_{0.2}Mn_{0.2}Co_{0.2}Ni_{0.2}Zn_{0.2}$ (MgMnCoNiZn), $Mg_{0.2}Mn_{0.2}Co_{0.2}Ni_{0.2}(Li_{0.1}Fe_{0.1})$ (MgMnCoNi(LiFe)), $Mn_{0.2}Co_{0.2}Ni_{0.2}Li_{0.2}Sc_{0.1}In_{0.1}$ (MnCoNiLi(ScIn)), and $Mg_{0.2}Co_{0.2}Ni_{0.2}Zn_{0.2}Li_{0.1}In_{0.1}$ (MgCoNiZn(LiIn)). For $(MgMnCoNiZn)TiO_3$, the selected reflection indices for the space group $R\bar{3}$ (No. 148) are indicated. (c) Lattice parameters of high-entropy ilmenite-type oxides as a function of the averaged ionic radii of the M cations, $\langle r_M \rangle$. The red (blue) markers represent the length of the *a*-axis (*c*-axis) of the unit cell, which refers to the left (right) vertical axis of the plot. The nominal chemical composition for each abbreviated sample name is given in Table 1.

https://doi.org/10.1021/acs.chemmater.6c01899
Chem. Mater. XXXX, XXX, XXX−XXX

Downloaded from pubs.acs.org/cmatex/article-pdf/doi/10.1021/acs.chemmater.6c01899/6839719/acs.chemmater.6c01899.pdf by NATL INST FOR MATLS SCIENCE (NIMS) user on 11 September 2026

2.2. Powder X-ray Diffraction

The products were characterized using powder X-ray diffraction (PXRD). The measurements were carried out using a Stoe Stadi-P diffractometer with monochromatic Mo−Kα_1 radiation from a primary Ge(111) Johannson-type monochromator or a Bruker D2 Phaser diffractometer with Cu−Kα radiation. The measurements with Stoe Stadi-P were performed in Debye-Scherrer geometry and the scattered X-rays were collected using a triple array of Mythen 1K detectors (Dectris). The samples were sealed in 0.3 mm diameter borosilicate glass capillaries that were spun during the measurements. A scan range from 2θ = 2° to 110° and a total scan time of 3 h was applied for every sample. The measurements with Bruker D2 Phaser were performed in Bragg-Brentano geometry, and the powder samples were placed on a flat Si sample holder, which was spun during the measurements. The lattice parameters were determined by fully weighted Rietveld refinements using TOPAS v.6.[20] The crystal structure of $CoTiO_3$ was used as the initial model.[21]

2.3. Energy-Dispersive X-ray Spectroscopy

The chemical compositions of the samples were examined using energy-dispersive X-ray spectroscopy (EDX) equipped with a SEM. A Tescan Vega4 LMU SEM instrument equipped with an Oxford X-Max^N 20 was used for the measurements. For each sample, 5−6 EDX spectra were measured at different spots.

2.4. X-ray Photoelectron Spectroscopy

X-ray photoelectron spectroscopy (XPS) analyses were performed using a Thermo K-Alpha+ spectrometer equipped with a monochromatic Al-Kα X-ray source (1486.7 eV) operated at 12 kV and 6 mA (72 W). The angle between the analyzer and the X-ray source was 56°. The X-ray spot size was 400 μm, corresponding to an irradiated area of approximately 0.1 mm^2. The base pressure in the analysis chamber was maintained at 2×10^{-9} mbar.

The spectrometer was calibrated using metallic reference samples of Cu, Ag, and Au, with binding energies set at 932.6 eV for Cu $2p_{3/2}$, 368.2 eV for Ag $3d_{5/2}$, and 84.0 eV for Au $4f_{7/2}$. Charge compensation was achieved using a dual-beam flood gun that provided low-energy electrons (<5 eV) under a partial argon atmosphere. Binding energy referencing was performed on the C−C component of the C 1s peak to 284.8 eV. The binding energy accuracy was ±0.2 eV.

Survey spectra were acquired at a pass energy of 200 eV with a step size of 1 eV and a dwell time of 10 ms per point. High-resolution spectra were recorded at a pass energy of 50 eV with a step size of 0.1 eV and a dwell time of 50 ms per point.

2.5. Magnetic and Thermodynamic Measurements

The magnetization of the samples was evaluated using a Quantum Design MPMS3. The data were collected from 2 to 350 K under a magnetic field of 0.1 T in both zero-field and field-cooled procedures. AC magnetic susceptibility measurements were performed using a Quantum Design MPMS-XL. An AC magnetic field of 4 Oe was applied in the 1−1000 Hz frequency range. The heat capacity, $C(T)$, was measured using a Quantum Design PPMS. The lattice contribution to $C(T)$ was evaluated by measuring the heat capacity of a non-magnetic $(Mg_{0.5}Zn_{0.5})TiO_3$ ilmenite sample. All measurements were performed on polycrystalline samples.

2.6. Powder Neutron Diffraction

Neutron diffraction measurements on $(MgMnCoNiZn)TiO_3$ were conducted at the time-of-flight neutron diffractometer GEM of ISIS Neutron and Muon Source, U.K.[22] A ∼6.0 g powder sample was loaded into a thin-wall vanadium can, and the data were collected from 1.85 to 20 K. The magnetic structure was analyzed using the SARAh[23] and FullProf Suite[24] programs. The chemical composition was fixed at the nominal one during the Rietveld refinement with FullProf.

3. RESULTS AND DISCUSSION

3.1. Long-Range Magnetic Order in High-Entropy Ilmenite $(MgMnCoNiZn)TiO_3$

The PXRD pattern of $(MgMnCoNiZn)TiO_3$ synthesized at 1100 °C in air is shown in Figure 1b. The observed pattern is consistent with an ilmenite-type structure (space group $R\bar{3}$, No. 148), with a minute amount of TiO_2 rutile impurities. The lattice parameters obtained by Rietveld refinement were a = 5.07544(3) Å and c = 13.96301(9) Å (Figure S1b of Supporting Information). No noticeable difference was found in the $(MgMnCoNiZn)TiO_3$ samples annealed under different conditions (Figure S2 of Supporting Information). The EDX measurement of the powder sample indicated a chemical composition close to the nominal ratio of M ions (Table S1 of Supporting Information), and the XPS measurements supported that the Mn, Co, and Ni ions at the M-site adopt divalent ionic states (Figure S4 of Supporting Information).

This ilmenite phase is most likely stabilized by its formation enthalpy, rather than by entropy stabilization. To confirm whether the ilmenite phase was entropy-stabilized, the high-entropy ilmenite sample was annealed at 850 °C in air. In contrast to the rocksalt $(MgCoNiCuZn)O$[3], the ilmenite sample did not decompose during the low-temperature annealing. This suggests that the ilmenite phase is predominantly stabilized by its formation enthalpy, although its high configuration entropy may play some role. We also attempted to synthesize a high-entropy ilmenite with a combination of the divalent cations similar to that used for rocksalt-type HEOx $(MgCoNiCuZn)O$. However, the product contained several impurity phases, such as TiO_2 rutile and M_2TiO_4 inverse spinel oxides. Therefore, in contrast to the rocksalt-type structure, it is not easy to fully accommodate the Jahn-Teller active Cu^{2+} ions into the ilmenite-type structure, likely due to the different bond geometries including face-shared bonds. Attempts to incorporate other divalent cations such as Cd^{2+} and Fe^{2+} were also unsuccessful.

The high-entropy ilmenite $(MgMnCoNiZn)TiO_3$ was found to exhibit long-range magnetic order. Magnetic susceptibility, $\chi(T)$, measured at a magnetic field of 0.1 T is shown in Figure 2a. A clear cusp was observed at 9.5 K in both the zero-field-cooled and field-cooled processes, indicating the appearance of antiferromagnetic order. A similar behavior of $\chi(T)$ was observed in the samples annealed in argon or oxygen gas flow, indicating that the potential influence of oxygen non-stoichiometry is negligible in the magnetic properties (Figure S3 of Supporting Information). The real part of the AC magnetic susceptibility, $\chi'(T)$, shows a sharp cusp near 9.5 K without any frequency dependence. This excludes the formation of a spin-glass state (Figure S5 of Supporting Information). The inset of Figure 2a shows the inverse of the magnetic susceptibility, $\chi^{-1}(T)$. The Curie-Weiss fit of $\chi^{-1}(T)$ above 250 K yields an effective moment, μ_{eff}, of 3.76 μ_B/f.u. and a negative Curie-Weiss temperature of θ_{CW} = −27 K. The magnitude of the effective moment agrees well with the expected value of 3.75 μ_B/f.u., which was estimated as $\mu_{eff} = \sqrt{0.2 \times \mu_{eff,Mn}^2 + 0.2 \times \mu_{eff,Co}^2 + 0.2 \times \mu_{eff,Ni}^2}$ using the effective moments of the parent compounds such as $MnTiO_3$ ($\mu_{eff,Mn}$ = 5.90 μ_B/Mn^{2+}),[25] $CoTiO_3$ ($\mu_{eff,Co}$ = 5.02 μ_B/Co^{2+}), and $NiTiO_3$ ($\mu_{eff,Ni}$ = 3.21 μ_B/Ni^{2+}).[26] A slight deviation from the Curie-Weiss behavior was observed in the $\chi^{-1}(T)$ profile below ∼100 K, implying the development of short-range

Downloaded from pubs.acs.org/cmatex/article-pdf/doi/10.1021/acs.chemmater.6c01899/6839719/acs.chemmater.6c01899.pdf by NATL INST FOR MATLS SCIENCE (NIMS) user on 11 September 2026

https://doi.org/10.1021/acs.chemmater.6c01899
Chem. Mater. XXXX, XXX, XXX−XXX

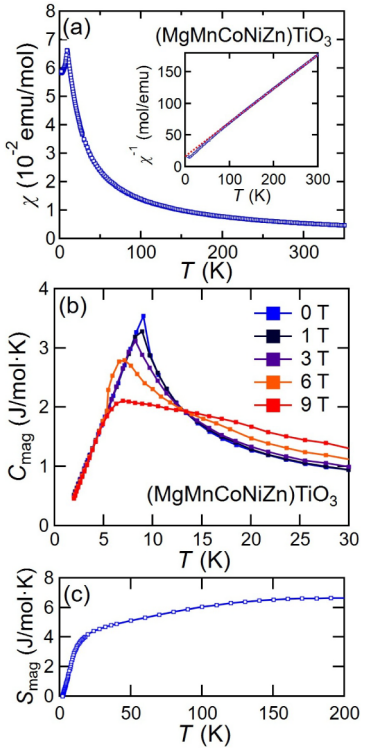


Figure 2. Magnetic and thermodynamic properties of the high-entropy ilmenite $(MgMnCoNiZn)TiO_3$. (a) Temperature dependence of magnetic susceptibility, $\chi(T)$, measured at a magnetic field of 0.1 T. The inset shows the temperature dependence of the inverse of magnetic susceptibility, $\chi^{-1}(T)$. The red-dotted line delineates the Curie-Weiss fit. (b) Magnetic specific heat, $C_{mag}(T)$, around the antiferromagnetic transition temperature T_N at zero and applied magnetic fields. The lattice contribution to the heat capacity was subtracted using the heat capacity of the non-magnetic ilmenite $(Mg_{0.5}Zn_{0.5})TiO_3$. (c) Magnetic entropy, S_{mag}, of $(MgMnCoNiZn)TiO_3$ at zero magnetic field estimated by integrating $C_{mag}(T)/T$.

magnetic correlations above T_N. The presence of long-range magnetic order was further corroborated by specific heat measurements. Figure 2b shows the magnetic specific heat, $C_{mag}(T)$, where the lattice contribution, $C_{ph}(T)$, to the total heat capacity was subtracted by using the $C(T)$ of the non-magnetic ilmenite $(Mg_{0.5}Zn_{0.5})TiO_3$ (Figure S6 of Supporting Information). $C_{mag}(T)$ of $(MgMnCoNiZn)TiO_3$ exhibited a sharp peak near 9.5 K. This ordering temperature is substantially lower than that of the parent ilmenite-type oxides such as T_N = 64 K for $MnTiO_3$[27] and T_N = 38 K for $CoTiO_3$.[26]

A remarkable feature of the specific heat of $(MgMnCoNiZn)TiO_3$ is that $C_{mag}(T)$ decreases at a moderate rate ($C_{mag} \sim T^{1.2}$) when cooled below T_N. $C_{mag}(T)$ of the parent ilmenites, such as $CoTiO_3$ and $NiTiO_3$, shows a much steeper decrease right below T_N (Ref. 26 and Figure S7 of Supporting Information). The behavior of $C_{mag}(T)$ for $(MgMnCoNiZn)TiO_3$ may be attributed to the presence of strong disorder in the magnetic sublattice, which may affect the magnon excitation spectrum, as observed in disordered antiferromagnets.[28,29]

The magnetic entropy, $S_{mag}(T)$, estimated by integrating $C_{mag}(T)/T$ at zero magnetic field is shown in Figure 2c. The total magnetic entropy expected in $(MgMnCoNiZn)TiO_3$ is approximately 5.96 J/mol·K from the presence of Mn^{2+} (S = 5/2 quintet), Co^{2+} (J_{eff} = 1/2 doublet),[30] and Ni^{2+} (S = 1 triplet) ions. The magnetic entropy shows a steep increase around T_N upon heating and gradually increases further above T_N up to ~100 K. This implies that the magnitude of the magnetic interactions is of the order of 100 K and short-range magnetic correlations develop at temperatures much higher than T_N. The smaller magnitude of the Curie-Weiss temperature, $|\theta_{CW}|$ = 27 K, can be ascribed to the coexistence of ferro- and antiferromagnetic interactions associated with the presence of multiple magnetic ions. The magnetic entropy at high temperatures exceeds the expected value of 5.96 J/mol·K. We suspect that this is caused by the thermal population of the excited J_{eff} = 3/2 levels of Co^{2+} ions.[31]

$C_{mag}(T)$ shows a strong magnetic-field dependence above 6 T. At low fields (up to 3 T), the peak value of $C_{mag}(T)$ at T_N was only moderately suppressed. $C_{mag}(T)$ was, however, substantially suppressed near T_N above 6 T, and some portions of the magnetic entropy were transferred to higher temperatures. This may be attributed to the presence of ferromagnetically correlated moments above T_N as inferred from the $\chi^{-1}(T)$ and $S_{mag}(T)$ data, and the partial alignment of magnetic moments takes place above T_N under high magnetic fields. Similarly, the sharp cusp of $\chi(T)$ at T_N was gradually smeared out by increasing the magnetic field, although no ferromagnetic behavior was seen up to 7 T (Figure S8 of Supporting Information for the magnetic susceptibility at high fields and the magnetization curve at 2 K). This suggests that ferromagnetically correlated moments are present at high temperatures but their long-range ordering may be hampered by bond-disorder.

3.2. Magnetic Structure of $(MgMnCoNiZn)TiO_3$

The magnetic structure of the high-entropy ilmenite $(MgMnCoNiZn)TiO_3$ is of particular interest regarding how the competing magnetic interactions, in the presence of strong chemical disorder, are reconciled. We studied this by powder neutron diffraction measurements at the GEM diffractometer of ISIS Neutron and Muon Source. The neutron diffraction pattern for the Bank 2 detector of the GEM diffractometer is displayed in Figure 3a, where an additional peak at a d-spacing of ~9.3 Å was observed clearly at 1.85 K. As shown in the inset, this peak began to grow right below T_N (~9.5 K), which is suggestive of a magnetic origin. Similar additional peaks were observed below T_N, as shown in Figure 3b. These peaks can be indexed with a propagation vector $\boldsymbol{k}$ = (0, 0, 3/2), which is identical to that of $CoTiO_3$ and $NiTiO_3$ forming an A-type antiferromagnetic order. The temperature dependence of the integrated intensity of the (0 0 3/2) magnetic Bragg reflection, $I(T)$, shown in Figure 3d, was fitted with a power-law function, $I(T) = I_0 (1 - T/T_N)^{2\beta}$. The fitting yields T_N = 10.0(1) K and β = 0.34(3). This value of β is close to that of the three-dimensional XY model (β = 0.345) and that obtained for $NiTiO_3$, β = 0.35(1),[32] suggesting a similar spin anisotropy.

From the space group of $R\bar{3}$ (No. 148) and the propagation vector, we constructed models of the possible magnetic structures with the help of the SARAh program.[23] There are six irreducible representations (Irreps) compatible with the propagation vector, as listed in Table 2. The Irreps are one-dimensional, and all the components of the basis vectors are real numbers. Among the Irreps, the Γ_3 and Γ_5 models are consistent with the observed magnetic Bragg reflections. The two basis vectors, Ψ_3 and Ψ_5, represent ferromagnetic ordering within the ab-planes, and the ferromagnetic planes stack antiferromagnetically along the c-axis, namely, the A-type

Downloaded from pubs.acs.org/cmatex/article-pdf/doi/10.1021/acs.chemmater.6c01899/6839719/acs.chemmater.6c01899.pdf by NATL INST FOR MATLS SCIENCE (NIMS) user on 11 September 2026

https://doi.org/10.1021/acs.chemmater.6c01899
Chem. Mater. XXXX, XXX, XXX−XXX

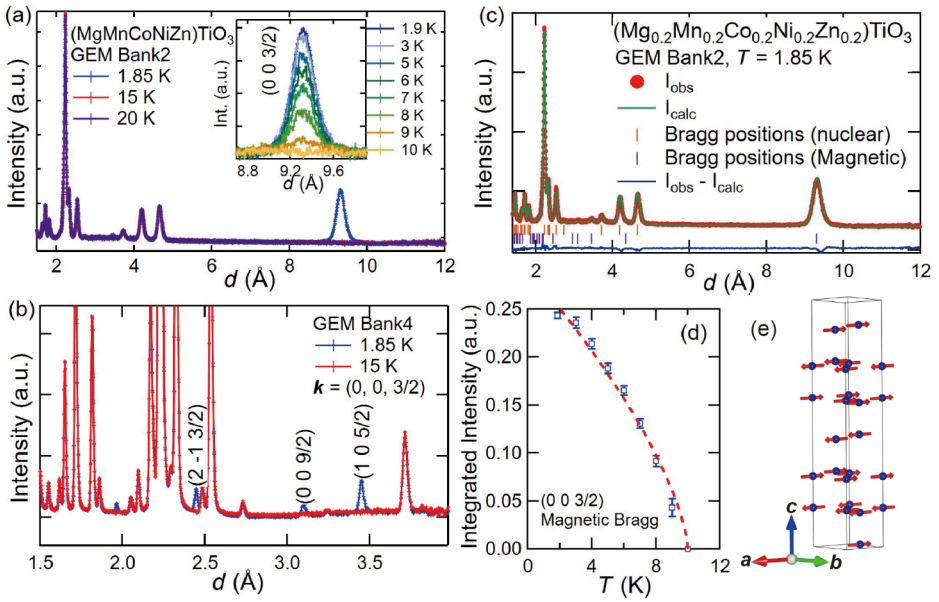


Figure 3. Powder neutron diffraction measurements and refined magnetic structure of $(MgMnCoNiZn)TiO_3$. (a) Powder neutron diffraction patterns recorded at Bank 2 of GEM diffractometer measured at 1.85, 15, and 20 K. An additional peak was seen at 1.85 K around the *d*-spacing of 9.3 Å. The inset shows the temperature dependence of the additional peak indexed as (0 0 3/2). (b) Powder diffraction patterns recorded at Bank 4 of GEM, collected at 1.85 and 15 K. The additional Bragg peaks at 1.85 K were indexed with a propagation vector $\boldsymbol{k} = (0, 0, 3/2)$. (c) Rietveld refinement of the powder neutron diffraction pattern (Bank 2, GEM) at 1.85 K. The refinement indices are $R_{Bragg} = 5.38\%$ and $R_F = 6.38\%$ for the nuclear structure, and the magnetic *R*-factor is $R = 13.3\%$. (d) Temperature dependence of the integrated intensity of magnetic (0 0 3/2) Bragg peak. The red-dashed line shows a power-law fit, $I(T) = I_0\,(1 - T/T_N)^{2\beta}$. (e) Refined magnetic structure of $(MgMnCoNiZn)TiO_3$. For brevity, only the M ions are displayed and they are all assumed to possess the same magnetic moments. The magnetic structure is identical with that of $CoTiO_3$, namely, an A-type antiferromagnetic order.

Table 1. Lattice Parameters of High-Entropy Ilmenites $MTiO_3$[a]

Nominal composition	Abbrev. name	$\langle r_M \rangle$ (Å)	σ^2 (10^{-4} Å^2)	*a* (Å)	*c* (Å)
$Mg_{0.2}Co_{0.2}Ni_{0.2}Zn_{0.2}Li_{0.1}Sc_{0.1}TiO_3$	MgCoNiZn(LiSc)	0.730	5.2	5.06223(4)	13.9195(2)
$Mg_{0.2}Co_{0.2}Ni_{0.2}Zn_{0.2}Li_{0.1}In_{0.1}TiO_3$	MgCoNiZn(LiIn)	0.735	9.6	5.07127(3)	13.9604(1)
$Mg_{0.2}Mn_{0.2}Co_{0.2}Ni_{0.2}Li_{0.1}Fe_{0.1}TiO_3$	MgMnCoNi(LiFe)	0.738	31.4	5.06694(3)	13.9379(1)
$Mg_{0.2}Mn_{0.2}Co_{0.2}Ni_{0.2}Zn_{0.2}TiO_3$	MgMnCoNiZn	0.745	21.8	5.07544(3)	13.96301(9)
$Mg_{0.2}Mn_{0.2}Co_{0.2}Ni_{0.2}Li_{0.1}Sc_{0.1}TiO_3$	MgMnCoNi(LiSc)	0.748	21.9	5.07434(3)	13.9925(1)
$Mg_{0.2}Mn_{0.2}Co_{0.2}Ni_{0.2}Li_{0.1}In_{0.1}TiO_3$	MgMnCoNi(LiIn)	0.753	24.3	5.08346(3)	14.03105(9)
$Mn_{0.2}Co_{0.2}Ni_{0.2}Li_{0.2}Sc_{0.1}In_{0.1}TiO_3$	MnCoNiLi(ScIn)	0.760	21.9	5.08774(3)	14.07867(9)

[a]Abbreviated sample names are used in Figures 1c and 4 and in Table 3. $\langle r_M \rangle$ represents the average of the ionic radii of the M-cations calculated using Shannon's ionic radii for octahedral coordination.[47] σ^2 indicates the size variance of the M-cation ionic radii, $\sigma^2 = \Sigma_i m_i (r_{M,i} - \langle r_M \rangle)^2$, where m_i represents the molar fraction of cation *i*.

antiferromagnetic order as in $CoTiO_3$ and $NiTiO_3$. The difference between Ψ_3 and Ψ_5 is only found in the direction of the magnetic moments lying in the *ab*-planes, which cannot be distinguished by powder neutron diffraction experiments. Thus, we used the Γ_3 model for refinement, where the magnetic moments are directed along the *a*-axis.

The result of the Rietveld refinement in the magnetically ordered phase at 1.85 K is shown in Figure 3c. In the refinement of the magnetic structure, for simplicity, we assumed that all M^{2+} cations possessed the same magnetic moments with a magnetic form factor of the Co^{2+} ion. The refined magnetic structure is depicted in Figure 3e. The magnitude of the ordered moment thus estimated is 0.66(1) μ_B/M^{2+}, which is much smaller than the average magnetic moments of ~1.83 μ_B, based on the 20% contributions from Mn^{2+} ($S = 5/2$, 5 μ_B), Co^{2+} ($J_{eff} = 1/2$ and $g = 4.33$,[33] ~2.17 μ_B), and Ni^{2+} ($S = 1$, 2 μ_B) ions. Reduced ordered moments have been observed in magnetic high-entropy compounds, possibly due to strong fluctuations associated with chemical disorder and magnetic bond-disorder.[11,34]

3.3. High-Entropy Ilmenites with Aliovalent Doping

The high-entropy ilmenite $(MgMnCoNiZn)TiO_3$ turned out to display long-range antiferromagnetic order, and its magnetic structure is identical with that of the parent $CoTiO_3$ and $NiTiO_3$ ilmenites. Meanwhile, the reduced magnitude of ordered magnetic moments suggests the presence of strong fluctuations associated with pronounced disorder. Thus, the enhancement of the chemical disorder may affect the magnetic ground state. As described above, $(MgMnCoNiZn)TiO_3$ is the only high-entropy ilmenite obtained by allocating divalent cations to the M-site in an equimolar ratio. Instead, one (or two) of the divalent cations was successfully replaced by an equimolar amount of monovalent Li^+ ions and a trivalent cation such as Fe^{3+}, Sc^{3+}, or In^{3+}, as in the case of the rocksalt-type high-entropy oxides.[5,11] Such aliovalent doping is expected to introduce extra disorder and local lattice distortion

https://doi.org/10.1021/acs.chemmater.6c01899
Chem. Mater. XXXX, XXX, XXX−XXX

Downloaded from pubs.acs.org/cmatex/article-pdf/doi/10.1021/acs.chemmater.6c01899/6839719/acs.chemmater.6c01899.pdf by NATL INST FOR MATLS SCIENCE (NIMS) user on 11 September 2026

induced by cations with different valence states.[35] The PXRD patterns of the aliovalent-doped samples are shown in Figure 1b and Figure S1a of Supporting Information. These samples formed a nearly single-phase of the ilmenite-type structure. The refined lattice parameters are listed in Table 1 and plotted with respect to the average ionic radii of M-cations, $\langle r_M \rangle$, in Figure 1c. The lattice parameters scaled nearly linearly with $\langle r_M \rangle$, suggesting that all the M-cations were successfully accommodated in the ilmenite structure.

Despite the enhanced chemical disorder, $\chi(T)$ of the aliovalent-doped samples showed a sharp cusp, similar to that of $(MgMnCoNiZn)TiO_3$ as shown in Figure 4a, indicative

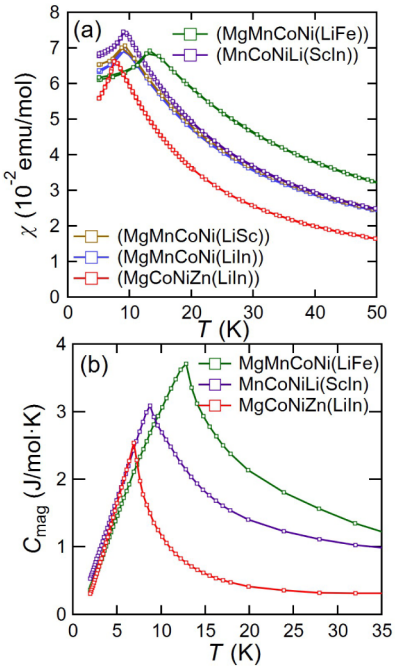


Figure 4. Magnetic properties of aliovalent-doped high-entropy ilmenites $MTiO_3$. (a) Magnetic susceptibility, $\chi(T)$, measured at 0.1 T. The nominal chemical composition of each sample is found in Table 1. (b) Magnetic specific heat, $C_{mag}(T)$, near the antiferromagnetic ordering temperature, T_N. For all the samples, the behaviors of $C_{mag}(T)$ below T_N are analogous to that of $(MgMnCoNiZn)TiO_3$.

of long-range antiferromagnetic order. The presence of long-range magnetic ordering was further confirmed by specific heat measurements. The magnetic specific heat, $C_{mag}(T)$, of $(MgMnCoNi(LiFe))TiO_3$, $(MnCoNiLi(ScIn))TiO_3$ and $(MgCoNiZn(LiIn))TiO_3$ are shown in Figure 4b, where the lattice contributions were subtracted using a procedure similar to that employed for $(MgMnCoNiZn)TiO_3$. $C_{mag}(T)$ below T_N appears to decrease nearly linearly with temperature, akin to $(MgMnCoNiZn)TiO_3$. The ordering temperature T_N and the Curie-Weiss temperature are summarized in Table 3. T_N appears to be solely determined by the contents of magnetic ions, and is independent of the identity of non-magnetic ions. That is, the average ionic radii or the variance of the ionic radii does not affect T_N, unlike other high-entropy oxides, where a large variance in the ionic radii tends to reduce the transition temperature.[36,37] We suspect that the local structural modulation induced by cations with different ionic radii or valence states may be moderate and its influence on the magnetic exchange paths is negligibly small in the ilmenite structure comprising a rigid structural network with edge- and face-shared bonds, compared to the corner-shared network of perovskite or pyrochlore oxides.

Interestingly, long-range order was found in $(MgCoNiZn(LiIn))TiO_3$ that contains only 40% magnetic cations at the M-site. We note that the 40% concentration of magnetic ions is far below the percolation threshold of a two-dimensional honeycomb lattice, which is approximately 69%. We speculate that the sizable interlayer coupling of the ilmenite structure, together with longer-range interactions within the honeycomb lattice, may facilitate long-range magnetic ordering.[38,39] Longer-range interactions are probably operative in all magnetic high-entropy ilmenites to stabilize the long-range order despite the presence of non-magnetic M cations, i.e., "magnetic vacancies". That is, even though nearest-neighbor magnetic interactions are disrupted by magnetic vacancies,

Table 2. Irreducible Representations (Irreps) and Basis Vectors (BV) for the M-Site Atom of $(MgMnCoNiZn)TiO_3$[a]

			BV components		
Irrep	BV	M-site	m_a	m_b	m_c
Γ_1	Ψ_1	1	0	0	3
		2	0	0	−3
Γ_2	Ψ_2	1	0	0	3
		2	0	0	3
Γ_3	Ψ_3	1	3	0	0
		2	−3	0	0
Γ_4	Ψ_4	1	3	0	0
		2	3	0	0
Γ_5	Ψ_5	1	−1.732	−3.464	0
		2	1.732	3.464	0
Γ_6	Ψ_6	1	−1.732	−3.464	0
		2	−1.732	−3.464	0

[a] $(MgMnCoNiZn)TiO_3$ crystallizes in a rhombohedral structure with space group of $R\bar{3}$ (No. 148) and the M ions occupy the 6*c* Wyckoff site, (0, 0, *z*), with $z = 0.3552(3)$. The propagation vector is $\boldsymbol{k} = (0, 0, 3/2)$. There are two distinct M-sites in the unit cell, located at 1: (0, 0, 0.3552) and 2: (0, 0, 0.6448). All the imaginary components of the basis vectors are zero.

Table 3. Magnetic Properties of High-Entropy Ilmenite-Type Oxides $MTiO_3$[a]

Abbrev. sample name	Ratio of magnetic M ions (%)	T_N (K)	μ_{eff} (μ_B/f.u.)	Expected μ_{eff} (μ_B/f.u.)	θ_{CW} (K)
MgMnCoNi(LiFe)	70	13.0	4.95	4.19	−83
MgMnCoNiZn	60	9.5	3.76	3.75	−27
MgMnCoNi(LiSc)	60	9.5	3.84	3.75	−32
MgMnCoNi(LiIn)	60	9.5	3.83	3.75	−32
MnCoNiLi(InSc)	60	9.5	3.82	3.75	−30
MgCoNiZn(LiIn)	40	7.5	2.84	2.66	−10

[a] The nominal chemical compositions of the samples are shown in Table 1. The table shows the antiferromagnetic ordering temperature T_N determined by the cusp of $\chi(T)$, effective moment μ_{eff}, and Curie-Weiss temperature θ_{CW} obtained from the Curie-Weiss fit of $\chi^{-1}(T)$. The expected μ_{eff} was calculated as $\mu_{eff} = \sqrt{\sum_i m_i \mu_{eff,i}^2}$, where m_i is a molar fraction of magnetic ion *i* and $\mu_{eff,i}$ is the effective moment of the magnetic ion. The reported values for $MnTiO_3$, $CoTiO_3$ and $NiTiO_3$ were used as $\mu_{eff,i}$ for Mn^{2+}, Co^{2+} and Ni^{2+} ions, respectively.[25,26] For Fe^{3+} ions, the value of $S = 5/2$ with a *g*-factor of 2, $\mu_{eff,Fe} = 5.92\ \mu_B$, was used.

Downloaded from pubs.acs.org/cmatex/article-pdf/doi/10.1021/acs.chemmater.6c01899/6839719/acs.chemmater.6c01899.pdf by NATL INST FOR MATLS SCIENCE (NIMS) user on 11 September 2026

https://doi.org/10.1021/acs.chemmater.6c01899
Chem. Mater. XXXX, XXX, XXX−XXX

magnetic correlations develop throughout the crystal via longer-range magnetic interactions.

3.4. Formation of a Spin-Glass State by Changing the Compositional Ratio of Magnetic Ions

The long-range magnetic order of the high-entropy ilmenites was found to be robust against aliovalent doping, which induces additional chemical disorder. In fact, the high-entropy ilmenite $(MgMnCoNiZn)TiO_3$ and those with aliovalent doping have larger amounts of magnetic ions that prefer in-plane ferromagnetic coupling, that is, Co^{2+} and Ni^{2+}, compared to those with dominant antiferromagnetic interactions, such as Mn^{2+} and probably isoelectronic Fe^{3+}. This may promote long-range magnetic order with in-plane ferromagnetic alignments. In an attempt to further enhance the competition of two different magnetic interactions, we synthesized a Mn-rich high-entropy ilmenite $(Mg_{0.2}Mn_{0.3}Co_{0.15}Ni_{0.15}Zn_{0.2})TiO_3$ with a (Co + Ni)/Mn ratio of unity (see Figure S9a of Supporting Information for the PXRD pattern).

In contrast to $(MgMnCoNiZn)TiO_3$ with equimolar amounts of the magnetic ions, the magnetic and thermodynamic properties of the Mn-rich sample indicated the formation of a spin-glass state. $\chi(T)$ shows a Curie-Weiss behavior at high temperatures as in other high-entropy ilmenites (Figure 5a). The Curie-Weiss fit yields an effective moment of ~3.96 μ_B/f.u. and a Curie-Weiss temperature θ_{CW} = −44 K (Figure S9b of Supporting Information). This value of the effective moment is close to the one expected from the chemical composition, μ_{eff} ~ 3.97 μ_B/f.u., indicating the successful incorporation of unequal amounts of the magnetic ions. θ_{CW} shifted to a larger negative value compared to that of the equimolar $(MgMnCoNiZn)TiO_3$ (θ_{CW} = −27 K), reflecting enhanced antiferromagnetic interactions with a larger amount of Mn^{2+} ions. A closer look at the low-temperature region revealed a bifurcation of $\chi(T)$ between the zero-field-cooled (ZFC) and the field-cooled (FC) data below 5 K. Additionally, the real part of the AC magnetic susceptibility, $\chi'(T)$, measured at zero external magnetic field shows a weak frequency dependence below the cusp at ~5 K (Figure 5b), unlike that of $(MgMnCoNiZn)TiO_3$. This suggests the formation of a spin-glass state below 5 K. $C_{mag}(T)$ of $(Mg_{0.2}Mn_{0.3}Co_{0.15}Ni_{0.15}Zn_{0.2})TiO_3$ shows a broad hump around 5 K instead of a sharp peak, which was gradually suppressed by increasing the magnetic fields, in line with a spin-glass state.

The $(Mg_{0.2}Mn_{0.3}Co_{0.15}Ni_{0.15}Zn_{0.2})TiO_3$ sample was therefore found to form a spin-glass state, unlike other high-entropy ilmenites. In mixed ilmenites with two magnetic ions, such as $Mn_{1-x}Ni_xTiO_3$, a spin-glass phase has been observed near x = 0.5, because of the competition between two distinct magnetic structures of Néel-type and A-type antiferromagnetic order.[40,41] Considering that both $CoTiO_3$ and $NiTiO_3$ form an identical in-plane ferromagnetic order, the chemical composition of $(Mg_{0.2}Mn_{0.3}Co_{0.15}Ni_{0.15}Zn_{0.2})TiO_3$ may be regarded as analogous to that of $Mn_{0.5}Ni_{0.5}TiO_3$ with a spin-glass ground state. The ground state of high-entropy ilmenites may be solely controlled by the compositional ratio of magnetic ions.

Nevertheless, we infer that the magnetic interactions in high-entropy ilmenites should be more subtle because of the presence of different types of magnetic interactions in the nearest-neighbor bonds, such as Mn−Mn, Mn−Co, Mn−Ni, Co−Co, Co−Ni, and Ni−Ni pairs. The magnetic interactions

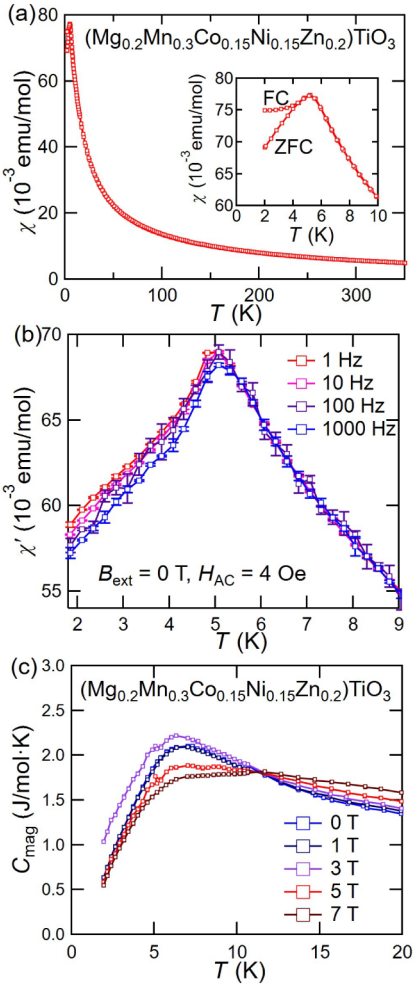


Figure 5. Magnetic and thermodynamic properties of the Mn-rich high-entropy ilmenite $(Mg_{0.2}Mn_{0.3}Co_{0.15}Ni_{0.15}Zn_{0.2})TiO_3$. (a) Temperature dependence of the magnetic susceptibility, $\chi(T)$. The inset shows a magnified view of the cusp at ~5 K. (b) The real part of the AC magnetic susceptibility, $\chi'(T)$, measured at zero external magnetic field. The AC magnetic fields of 4 Oe were applied at the frequency of 1, 10, 100, and 1000 Hz. (c) Magnetic heat capacity, $C_{mag}(T)$, at low temperatures. The lattice specific heat was subtracted using the heat capacity of the non-magnetic $(Mg_{0.5}Zn_{0.5})TiO_3$. A broad hump centered at ~5 K was gradually suppressed by increasing magnetic fields, supporting a spin-glass state.

in the Co−Co, Co−Ni, and Ni−Ni pairs of the edge-shared 90° bonds should be ferromagnetic due to the superexchange interactions of e_g electrons, whereas the Mn−Mn bond yields antiferromagnetic interactions owing to the predominant direct hopping of t_{2g} electrons across the edges of the MnO_6 octahedra. The magnetic interactions in the Mn−Co and Mn−Ni pairs are multifaceted because of the existence of different hopping processes of d-electrons, such as $e_g - e_g$ or $t_{2g} - e_g$ orbitals. In addition, the hopping process between the $t_{2g} - t_{2g}$ orbitals is also active for the Mn−Co pair; the Mn−Co and Mn−Ni magnetic interactions are not thus fully identical, introducing additional competition in the high-entropy ilmenites. We suspect that such complex magnetic interactions lead to distinct magnetic properties in high-entropy ilmenites. Indeed, the suppression of ordered moments is much more pronounced in the high-entropy sample, compared to the mixed ilmenite $Mn_{1-x}Ni_xTiO_3$,[42] pointing to stronger magnetic

https://doi.org/10.1021/acs.chemmater.6c01899
Chem. Mater. XXXX, XXX, XXX−XXX

Downloaded from pubs.acs.org/cmatex/article-pdf/doi/10.1021/acs.chemmater.6c01899/6398719/acs.chemmater.6c01899.pdf by NATL INST FOR MATLS SCIENCE (NIMS) user on 11 September 2026

fluctuations. Since the mixed ilmenite $Mn_{1-x}Ni_xTiO_3$ displays rich magnetic phases in the intermediate x values, such as spin-reorientation transition,[40,42] more complex high-entropy ilmenites may potentially exhibit even richer magnetic behaviors via fine adjustment of the ratio of magnetic ions, which are worthy of further exploration.

4. CONCLUSION

High-entropy ilmenite-type oxides $MTiO_3$ with more than five different cations at the M-site were successfully synthesized. Despite the presence of strong cation disorder that leads to bond-disorder in magnetic exchange interactions, long-range antiferromagnetic order was identified in $(MgMnCoNiZn)TiO_3$ by the magnetic susceptibility, specific heat, and neutron diffraction measurements. Long-range magnetic ordering was retained in the presence of additional disorder introduced by aliovalent doping. We suspect that the robustness of the long-range magnetic order may be attributed to the presence of longer-range magnetic interactions and the rigid lattice of the ilmenite structure evading local distortion potentially induced by aliovalent doping. On the other hand, by changing the ratio of magnetic ions, spin-glass freezing was observed, likely owing to the enhanced competition of distinct magnetic interactions. This indicates that magnetic ground states of the high-entropy ilmenites can be controlled by the ratio of magnetic ions and rich magnetic phases may be realized by fine-tuning of competing magnetic interactions. Furthermore, ilmenite compounds have been reported to display a variety of functional properties, including magnetoelectric effect,[27,41] ferro-axial order,[43] toroidicity[44] and nontrivial topological magnetic excitations.[30,45] Exploring these properties in high-entropy ilmenites can be an intriguing future subject.

■ ASSOCIATED CONTENT

Supporting Information

The Supporting Information is available free of charge at https://pubs.acs.org/doi/10.1021/acs.chemmater.6c01899.

Powder X-ray diffraction patterns of all samples; Rietveld refinement; chemical characterization (EDX, XPS); annealing effects; AC magnetic susceptibility; specific heat; magnetization curve; additional characterization of the Mn-rich sample (PDF)

■ AUTHOR INFORMATION

Corresponding Authors

Tomohiro Takayama − *Max Planck Institute for Solid State Research, Stuttgart 70569, Germany; Institute for Functional Matter and Quantum Technologies, University of Stuttgart, Stuttgart 70569, Germany; National Institute for Materials Science, Tsukuba, Ibaraki 305-0047, Japan;* orcid.org/0000-0002-3492-2025; Email: TAKAYAMA.Tomohiro@nims.go.jp

Damian Contant − *Max Planck Institute for Solid State Research, Stuttgart 70569, Germany; Department of Chemistry, ENS Paris-Saclay, Université Paris-Saclay, Gif-sur-Yvette 91192, France;* Present Address: Department of Physics, King's College London, Strand, London, WC2R 2LS, U.K; Email: damian.contant@kcl.ac.uk

Sebastian Bette − *Max Planck Institute for Solid State Research, Stuttgart 70569, Germany*; Email: S.Bette@fkf.mpg.de

Robert Dinnebier − *Max Planck Institute for Solid State Research, Stuttgart 70569, Germany*; Email: R.Dinnebier@fkf.mpg.de

Hidenori Takagi − *Max Planck Institute for Solid State Research, Stuttgart 70569, Germany; Institute for Functional Matter and Quantum Technologies, University of Stuttgart, Stuttgart 70569, Germany; Department of Physics, University of Tokyo, Bunkyo, Tokyo 113-0033, Japan; National Institute for Materials Science, Tsukuba, Ibaraki 305-0047, Japan*; Email: H.Takagi@fkf.mpg.de

Authors

Ivan da Silva − *ISIS Neutron and Muon Source, STFC Rutherford Appleton Laboratory, Didcot, Oxon OX11 0QX, U.K.;* orcid.org/0000-0002-4472-9675

Diana Dragoe − *Institute of Molecular Chemistry and Materials of Orsay, UMR 8182 CNRS, Université Paris-Saclay, Orsay 91190, France;* orcid.org/0000-0002-8536-1205

Nita Dragoe − *Institute of Molecular Chemistry and Materials of Orsay, UMR 8182 CNRS, Université Paris-Saclay, Orsay 91190, France*

Complete contact information is available at: https://pubs.acs.org/10.1021/acs.chemmater.6c01899

Funding

Open access funding provided by Max Planck Society.

Notes

The authors declare no competing financial interest.

■ ACKNOWLEDGMENTS

We thank D. Bérardan and F. Orlandi for valuable discussions. We are grateful to V. Duppel and E. Bruecher for their experimental support. We acknowledge the provision of beamtime on GEM at the ISIS Neutron and Muon Source (Proposal No. RB2300010).[46] D.C. acknowledges the ARPE program of ENS Paris-Saclay for support during his stay at the Max Planck Institute for Solid State Research. This work was supported by the Deutsche Forschungsgemeinschaft (DFG), Project No. TA1086/1-1.

■ REFERENCES

(1) Yeh, J.-W.; Chen, S.-K.; Lin, S.-J.; Gan, J.-Y.; Chin, T.-S.; Shun, T.-T.; Tsau, C.-H.; Chang, S.-Y. Nanostructured high-entropy alloys with multiple principal elements: Novel alloy design concepts and outcomes. *Adv. Eng. Mater.* **2004**, *6*, 299−303.

(2) George, E. P.; Raabe, D.; Ritchie, R. O. High-entropy alloys. *Nat. Rev. Mater.* **2019**, *4*, 515−534.

(3) Rost, C. M.; Sachet, E.; Borman, T.; Moballegh, A.; Dickey, E. C.; Hou, D.; Jones, J. L.; Curtarolo, S.; Maria, J.-P. Entropy-stabilized oxides. *Nat. Commun.* **2015**, *6*, 8485.

(4) Musicó, B. L.; Gilbert, D.; Ward, T. Z.; Page, K.; George, E.; Yan, J.; Mandrus, D.; Keppens, V. The emergent field of high entropy oxides: Design, prospects, challenges, and opportunities for tailoring material properties. *APL Mater.* **2020**, *8*, 040912.

(5) Bérardan, D.; Franger, S.; Dragoe, D.; Meena, A. K.; Dragoe, N. Colossal dielectric constant in high entropy oxides. *Phys. Status Solidi RRL* **2016**, *10*, 328−333.

(6) Bérardan, D.; Franger, S.; Meena, A. K.; Dragoe, N. Room temperature lithium superionic conductivity in high entropy oxides. *J. Mater. Chem. A* **2016**, *4*, 9536−9541.

(7) Sarkar, A.; Velasco, L.; Wang, D.; Wang, Q.; Talasila, G.; de Biasi, L.; Kübel, C.; Brezesinski, T.; Bhattacharya, S. S.; Hahn, H.;

Downloaded from pubs.acs.org/cmatex/article-pdf/doi/10.1021/acs.chemmater.6c01899/6839719/acs.chemmater.6c01899.pdf by NATL INST FOR MATLS SCIENCE (NIMS) user on 11 September 2026

et al. High entropy oxides for reversible energy storage. *Nat. Commun.* **2018**, *9*, 3400.
(8) Lun, Z.; Ouyang, B.; Kwon, D.-H.; Ha, Y.; Foley, E. E.; Huang, T.-Y.; Cai, Z.; Kim, H.; Balasubramanian, M.; Sun, Y.; et al. Cation-disordered rocksalt-type high-entropy cathodes for Li-ion batteries. *Nat. Mater.* **2021**, *20*, 214−221.
(9) Wang, T.; Chen, H.; Yang, Z.; Liang, J.; Dai, S. High-entropy perovskite fluorides: A new platform for oxygen evolution catalysis. *J. Am. Chem. Soc.* **2020**, *142*, 4550−4554.
(10) Jiang, B.; Yu, Y.; Cui, J.; Liu, X.; Xie, L.; Liao, J.; Zhang, Q.; Huang, Y.; Ning, S.; Jia, B.; et al. High-entropy-stabilized chalcogenides with high thermoelectric performance. *Science* **2021**, *371*, 830−834.
(11) Jimenez-Segura, M. P.; Takayama, T.; Bérardan, D.; Hoser, A.; Reehuis, M.; Takagi, H.; Dragoe, N. Long-range magnetic ordering in rocksalt-type high-entropy oxides. *Appl. Phys. Lett.* **2019**, *114*, 122401.
(12) Zhang, J.; Yan, J.; Calder, S.; Zheng, Q.; McGuire, M. A.; Abernathy, D. L.; Ren, Y.; Lapidus, S. H.; Page, K.; Zheng, H.; et al. Long-range antiferromagnetic order in a rocksalt high-entropy oxide. *Chem. Mater.* **2019**, *31*, 3705−3711.
(13) Witte, R.; Sarkar, A.; Kruk, R.; Eggert, B.; Brand, R. A.; Wende, H.; Hahn, H. High-entropy oxides: An emerging prospect for magnetic rare-earth transition metal perovskites. *Phys. Rev. Mater.* **2019**, *3*, 034406.
(14) Sharma, Y.; Mazza, A. R.; Musico, B. L.; Skoropata, E.; Nepal, R.; Jin, R.; Ievlev, A. V.; Collins, L.; Gai, Z.; Chen, A.; et al. Magnetic texture in insulating single crystal high entropy oxide spinel films. *ACS Appl. Mater. Interfaces* **2021**, *13*, 17971−17977.
(15) Vayer, F.; Decorse, C.; Bérardan, D.; Dragoe, N. New entropy-stabilized oxide with pyrochlore structure: $Dy_2(Ti_{0.2}Zr_{0.2}Hf_{0.2}Ge_{0.2}Sn_{0.2})_2O_7$. *J. Alloys Comp.* **2021**, *883*, 160773.
(16) Sarkar, A.; Kruk, R.; Hahn, H. Magnetic properties of high entropy oxides. *Dalton Trans.* **2021**, *50*, 1973−1982.
(17) Rák, Z.; Brenner, D. W. Exchange interactions and long-range magnetic order in the (Mg, Co, Cu, Ni, Zn)O entropy-stabilized oxide: A theoretical investigation. *J. Appl. Phys.* **2020**, *127*, 185108.
(18) Shirane, G.; Pickart, S. J.; Ishikawa, Y. Neutron diffraction study of antiferromagnetic $MnTiO_3$ and $NiTiO_3$. *J. Phys. Soc. Jpn.* **1959**, *14*, 1352−1360.
(19) Newnham, R. E.; Fang, J. H.; Santoro, R. P. Crystal structure and magnetic properties of $CoTiO_3$. *Acta Crystallogr.* **1964**, *17*, 240−242.
(20) Coelho, A. A. TOPAS and TOPAS-Academic: an optimization program integrating computer algebra and crystallographic objects written in C++. *J. Appl. Crystallogr.* **2018**, *51*, 210−218.
(21) Kidoh, K.; Tanaka, K.; Marumo, F.; Takei, H. Electron density distribution in an ilmenite-type crystal of cobalt(II). titanium(IV) trioxide. *Acta Crystallogr.* **1984**, *B40*, 92−96.
(22) Hannon, A. C. Results on disordered materials from the GEneral Materials diffractometer, GEM, at ISIS. *Nucl. Instrum. Methods Phys. Res., Sect. A* **2005**, *551*, 88−107.
(23) Wills, A. S. A new protocol for the determination of magnetic structures using simulated annealing and representational analysis (SARAh). *Phys. B* **2000**, *276-278*, 680−681.
(24) Rodríguez-Carvajal, J. Recent advances in magnetic structure determination by neutron powder diffraction. *Phys. B* **1993**, *192*, 55−69.
(25) Yamauchi, H.; Hiroyoshi, H.; Yamada, M.; Watanabe, H.; Takei, H. Spin flopping in $MnTiO_3$. *J. Magn. Magn. Mater.* **1983**, *31-34*, 1071−1072.
(26) Harada, J. K.; Balhorn, L.; Hazi, J.; Kemei, M. C.; Seshadri, R. Magnetodielectric coupling in the ilmenites $MTiO_3$ (M = Co, Ni). *Phys. Rev. B* **2016**, *93*, 104404.
(27) Mufti, N.; Blake, G. R.; Mostovoy, M.; Riyadi, S.; Nugroho, A. A.; Palstra, T. T. M. Magnetoelectric coupling in $MnTiO_3$. *Phys. Rev. B* **2011**, *83*, 104416.
(28) Buyers, W. J. L.; Holden, T. M.; Svensson, E. C.; Cowley, R. A.; Stevenson, R. W. H. Character of excitations in substitutionally disordered antiferromagnets. *Phys. Rev. Lett.* **1971**, *27*, 1442.
(29) Cao, Y.; Liu, X.; Xu, W.; Yin, W.-G.; Meyers, D.; Kim, J.; Casa, D.; Upton, M. H.; Gog, T.; Berlijn, T.; et al. Giant spin gap and magnon localization in the disordered Heisenberg antiferromagnet $Sr_2Ir_{1-x}Ru_xO_4$. *Phys. Rev. B* **2017**, *95*, 121103.
(30) Yuan, B.; Khait, I.; Shu, G.-J.; Chou, F. C.; Stone, M. B.; Clancy, J. P.; Paramekanti, A.; Kim, Y.-J. Dirac magnons in a honeycomb lattice quantum XY magnet $CoTiO_3$. *Phys. Rev. X* **2020**, *10*, 011062.
(31) Ferreira-Carvalho, M. M.; Chen, S. H.; Ku, Y. C.; Jose, A.; Morrow, R.; Kuo, C. Y.; Chang, C. F.; Hu, Z.; Haverkort, M. W.; Tjeng, L. H. Direct evidence of a near-ideal $J_{eff} = 1/2$ ground state in triangular-lattice $Na_2BaCo(PO_4)_2$. *Phys. Rev. Mater.* **2026**, *10*, 025004.
(32) Dey, K.; Sauerland, S.; Ouladdiaf, B.; Beauvois, K.; Wadepohl, H.; Klingeler, R. Magnetostructural coupling in ilmenite-type $NiTiO_3$. *Phys. Rev. B* **2021**, *103*, 134438.
(33) Abragam, A.; Bleaney, B. *Electron Paramagnetic Resonance of Transition Ions*; Clarendon Press, 1970.
(34) Shen, Y.; Zhang, G.; Zhang, Q.; Gui, X.; Zhang, Y.; Lee, H.; Kuo, C.-T.; Lee, J.-S.; Sutarto, R.; Ye, F.; et al. Long-range magnetic order with disordered spin orientations in a high-entropy antiferromagnet. *Nat. Commun.* **2026**, *17*, 3558.
(35) Braun, J. L.; Rost, C. M.; Lim, M.; Giri, A.; Olson, D. H.; Kotsonis, G. N.; Stan, G.; Brenner, D. W.; Maria, J.-P.; Hopkins, P. E. Charge-induced disorder controls the thermal conductivity of entropy-stabilized oxides. *Adv. Mater.* **2018**, *30*, 1805004.
(36) Mazza, A. R.; Acharya, S. R.; Wąsik, P.; Lapano, J.; Li, J.; Musico, B. L.; Keppens, V.; Nelson, C. T.; May, A. F.; Brahlek, M.; et al. Variance induced decoupling of spin, lattice, and charge ordering in perovskite nickelates. *Phys. Rev. Res.* **2023**, *5*, 013008.
(37) Contant, D.; McNally, G. M.; Krajewska, A.; Takagi, H.; Takayama, T. Robust electronic phase transition against cation disorder in high-entropy pyrochlore iridates. *AIP Adv.* **2024**, *14*, 085316.
(38) Hwang, I. Y.; Lee, K. H.; Chung, J.-H.; Ikeuchi, K.; Garlea, V. O.; Yamauchi, H.; Akatsu, M.; Shamoto, S. Spin wave excitations in honeycomb antiferromagnet $MnTiO_3$. *J. Phys. Soc. Jpn.* **2021**, *90*, 064708.
(39) Das, S.; Voleti, S.; Saha-Dasgupta, T.; Paramekanti, A. XY magnetism, Kitaev exchange, and long-range frustration in the $J_{eff} = 1/2$ honeycomb cobaltates. *Phys. Rev. B* **2021**, *104*, 134425.
(40) Yoshizawa, H.; Kawano, H.; Mori, H.; Mitsuda, S.; Ito, A. Phase diagram of a Heisenberg-like spin glass $Ni_xMn_{1-x}TiO_3$. *Phys. B* **1992**, *180-181*, 94−96.
(41) Yamaguchi, Y.; Nakano, T.; Nozue, Y.; Kimura, T. Magneto-electric effect in an XY-like spin glass system $Ni_xMn_{1-x}TiO_3$. *Phys. Rev. Lett.* **2012**, *108*, 057203.
(42) Chi, S.; Ye, F.; Zhou, H. D.; Choi, E. S.; Hwang, J.; Cao, H.; Fernandez-Baca, J. A. Magnetoelectric coupling tuned by competing anisotropies in $Mn_{1-x}Ni_xTiO_3$. *Phys. Rev. B* **2014**, *90*, 144429.
(43) Hayashida, T.; Kimura, K.; Kimura, T. Electric field−induced magnetochiral dichroism in a ferroaxial crystal. *Proc. Natl. Acad. Sci. U. S. A.* **2023**, *120*, No. e2303251120.
(44) Du, K.; Jo, D.; Xu, X.; Huang, F.-T.; Lee, M.-H.; Chu, M.-W.; Wang, K.; Guo, X.; Zhao, L.; Vanderbilt, D.; et al. Electric toroidal invariance generates distinct transverse electromagnetic responses. *Nat. Phys.* **2026**, *22*, 61−67.
(45) Elliot, M.; McClarty, P. A.; Prabhakaran, D.; Johnson, R. D.; Walker, H. C.; Manuel, P.; Coldea, R. Order-by-disorder from bond-dependent exchange and intensity signature of nodal quasiparticles in a honeycomb cobaltate. *Nat. Commun.* **2021**, *12*, 3936.
(46) Takayama, T.; da Silva, I. *Magnetic structure analysis of ilmenite-type high-entropy oxide*; STFC ISIS Neutron and Muon Source. 2023.
(47) Shannon, R. D. Revised effective ionic radii and systematic studies of interatomic distances in halides and chalcogenides. *Acta Crystallogr.* **1976**, *A32*, 751−767.
(48) Momma, K.; Izumi, F. VESTA3 for three-dimensional visualization of crystal, volumetric and morphology data. *J. Appl. Crystallogr.* **2011**, *44*, 1272−1276.

Downloaded from pubs.acs.org/cmatex/article-pdf/doi/10.1021/acs.chemmater.6c01899/6839719/acs.chemmater.6c01899.pdf by NATL INST FOR MATLS SCIENCE (NIMS) user on 11 September 2026